# Sn-doped and porogen-modified TiO2 photocatalyst for solar light elimination of sulfure diethyle as a model for chemical warfare agent

Armelle Sengele, Didier Robert, Nicolas Keller, Christophe Colbeau-Justin, Valérie Keller

Applied Catalysis B: Environmental 245 (2019) 279–289

Contents lists available at ScienceDirect

Applied Catalysis B: Environmental

journal homepage: www.elsevier.com/locate/apcatb

# Sn-doped and porogen-modified $TiO_2$ photocatalyst for solar light elimination of sulfure diethyle as a model for chemical warfare agent

Armelle Sengele[a], Didier Robert[a,*], Nicolas Keller[a], Christophe Colbeau-Justin[b], Valérie Keller[a]

[a] ICPEES, Institut de Chimie et des Procédés pour l'Energie, l'Environnement et la Santé, CNRS, Université de Strasbourg, 25 rue Becquerel, 67087, Strasbourg Cedex, France

[b] Laboratoire de Chimie Physique, CNRS UMR 8000, Université Paris-Sud, 91405, Orsay Cedex, France

ARTICLE INFO

*Keywords:*
Sn-doped $TiO_2$
PEG-modified $TiO_2$
DES elimination
UV-A and solar light activation

ABSTRACT

In the context of the increase in chemical threat due to warfare agents, the development of efficient methods for destruction of Chemical Warfare Agents are of first importance both for civilian and military purposes. Here, we demonstrate that optimized Sn-$TiO_2$ doped and PEG-modified photocatalysts allow increased and high performances under UV−A and solar-light irradiations leading to total elimination of highly contaminated environments containing Diethylsulfide (DES) used as a model molecule mimicking Yperite (Mustard Gas). It has been shown that Sn doping induces significant modifications on the structural, morphological, surface, electronic and optical properties of $TiO_2$. For example, the addition of 1% Sn increases significantly the surface area from 30 to 80 $m^2/g$ and decreases the particle size, while Sn-doping results in a reduction of the anatase band-gap from 3.2 to 2.95 eV. Total DES elimination could be reached for 90 and 120 min under continuous contaminant flux under UV−A and solar light activation, respectively accompanied with limited deactivation phenomenon. Correlations between the resulting physico-chemical properties of the doped and PEG-modified materials and the photocatalytic activities were carried out. The results open up extremely promising way for the decontamination of highly contaminated environments containing real warfare agents under UV−A but also under solar light illumination.

## 1. Introduction

The risk of hazardous, toxic or lethal chemical dispersion has become a growing threat, increasing strongly the potential risks of exposure to toxic materials, in civilian as well as in military areas. It is thus necessary to elaborate efficient materials for suitable decontamination and protection of the population, especially in indoor places. The current methods investigated are incineration, destruction, neutralization using various chemicals [1] and adsorption of the contaminants by an adsorbant. Amongst the current methods investigated or used, *i.e.* incineration, destruction and neutralization using chemicals and adsorption, all present drawbacks: either they cannot be directly applied on the contaminated area or they do not lead to destruction of the toxic agent but rather only to an adsorption or a skin barrier protection effect. In some cases, the decontamination methods must be implemented after the event and after first-responder intervention, so that, till the decontamination technology can operate the risk remains with continuous hazards towards the contaminated places, the surrounding people and stakeholders. Amongst possible methods for destruction of CWAs, photocatalytic oxidation is a promising one [2]. One of the main advantages of photocatalysis compared to combustion or thermal oxidation catalysis is to operate at room temperature thus allowing to be applied in remote places or indoor environments where no heating facilities are available. Photocatalysis has already been successfully used for degradation of organosulfur compounds such as dietlhylsulfide (DES) [3–5] or 2-phenethyl-2-chloroethyl sulfide [6,7] acting as a simulant for the live blister mustard gas or nauseous organosulfides like dimethylsulfide [8,9]. However, these applications remain scare for the real live blister Yperite CWA [10–12]. It must be kept in mind that total oxidation of these toxic molecules induces the formation of gaseous $SO_2$ or sulfate residues. The main limitation when using photocatalysis for the oxidation of sulfur-containing organic molecules is the formation of sulfates as ultimate oxidation products, leading consequently to the deactivation of the photocatalytic active sites. The main challenge stays in delaying the deactivation due to sulfates accumulation while avoiding incomplete toxic by-products and hazardous $SO_2$ production. This point may be overcome by increasing the surface area, thus allowing to accumulate a larger amount of deposited sulfate species

* Corresponding author.
*E-mail address:* didier.robert@univ-lorraine.fr (D. Robert).

https://doi.org/10.1016/j.apcatb.2018.12.071
Received 27 September 2018; Received in revised form 23 December 2018; Accepted 27 December 2018
Available online 28 December 2018

before deactivation. Amongst different strategies to reach this goal, one can mention the use of a porogen-assisted $TiO_2$ synthesis or $TiO_2$ metal cationic doping. 4d and 5d cationic doping (Ta, Nb, W, Mo, …) consisting in the substitution of $Ti^{4+}$ by $M^{n+}$ in its lattice positions has already been identified as yielding an enhanced surface specific area [13]. In addition, in the case of Sn doping and due to small lattice mismatch between $TiO_2$ and $SnO_2$, an easy incorporation of Sn into $TiO_2$ lattice may take place and result in lowering its band gap [14–16]. Furthermore, the concentration of the cationic dopant has to be optimized to achieve high quality and efficient photocatalytic properties. Alternatively, a porogen-templated $TiO_2$ synthesis approach, induced by specific organic-inorganic interactions during synthesis results in the formation of uniform and tunable pores. Depending on the porogen used, the strategy of porogen assisted-synthesis may result in structured porous materials with increased surface areas [17–19].

In this paper, Sn-doped and PEG (PolyEthylenGlycol)-modified $TiO_2$ photocatalyst are elaborated using a modified sol-gel synthesis. The obtained materials are characterized in details from structural, morphological, surface properties and optical point of view. The impact of Sn content, of calcination temperature and of porogen content is analyzed and correlated to the UV-A and solar light photo-oxidation of DiethylSulfide (DES), a relevant model molecule for the Yperite chemical warfare agent.

## 2. Experimental

### 2.1. Photocatalyst preparation

Undoped and Sn-doped photocatalysts were synthesized by the same sol-gel method. 18.6 ml of titanium isopropoxide (Sigma-Aldrich, purity 97%) was mixed with 40 ml of absolute ethanol (purity 99.8%) at ambient temperature. Then 40 ml of water was added dropwise and the pH was adjusted around 9 by adding ammonia (Carlo Erba, 30% aqueous solution). The solution was left under agitation until dry paste was obtained which was further dried overnight at 100 °C. The obtained powder was calcined at 380 °C or 500 °C in static air for 3 h with a heating rate of 5 °C/min.

Sn-doped $TiO_2$ was obtained by dissolving $SnCl_4$ (Sigma-Aldrich, purity 99%) into the ethanol before mixing with titanium isopropoxide to achieve the required Sn:$TiO_2$ weight ratio (0.0243 ml of $SnCl_4$ for 0.5 wt.%, 0.0486 ml for 1 wt.%, 0.1942 ml for 4 wt.% and 0.3884 ml for 8 wt.%). To compare $TiO_2$ samples with pure tin oxide, $SnO_2$ was prepared using the same experimental protocol than the one carried out for $TiO_2$ sol-gel synthesis. $SnCl_4$ was dissolved in ethanol, the same volume of distilled water was added as well as a few drops of ammonia. The solution was evaporated at room temperature under stirring. The obtained powder was dried in an oven at 100 °C and then calcined at 500 °C in static air for 3 h with a heating rate of 5 °C/min. A white powder was obtained.

The samples made with a porogen follow the same synthesis. The porogen, PEG 4000 (Merck), was dispersed before all reagents in ethanol at different PEG:$TiO_2$ mass ratio (5 g of PEG for 1:1, 10 g for 2:1, 25 g for 5:1 and 35 g for 7:1). These samples were then calcinated in a vertical oven with a filter, so that the PEG residues can be separated from the $TiO_2$ powder, at 500 °C using an air flow of 50 ml/min for 3 h with a heating rate of 5 °C/min.

### 2.2. Characterization techniques

Surface area and porosity measurements were carried out on a ASAP2010 Micromeritics Tristar apparatus using $N_2$ as adsorbant at liquid $N_2$ temperature. Before $N_2$ adsorption, the material was outgassed under primary vacuum at 200 °C overnight. The specific surface area was calculated from the $N_2$ adsorption isotherm using the BET method, the micropore surface area was derived using the t-plot method, and the pore size distribution was obtained using the BJH method during the adsorption step.

Thermal Gravimetry Analysis (TGA) was performed using a TGA 5000 thermo-analyser. Each sample was placed in a platinum crucible and heated from room temperature to 800 °C with a heating rate of 15 °C/min, using a 20/80 vol.%/vol.% $O_2/N_2$ mixture at a flow rate of 25 mL/min.Temperature Programmed Oxidation (TPO) coupled to Mass Spectrometry analysis was also performed with a heating rate of 5 °C/min, using a 1% (v/v) $O_2$/He mixture at a flow rate of 25 mL/min.

Temperature Programmed Oxidation coupled with a mass spectrometer (TPO-MS) was performed using a Micromeritics AutoChem II chemisorptions analyser and a Pfeiffer Vacuum OmniStar™ mass spectrometer. Each sample was placed in a quartz tube and heated from room temperature to 1000 °C with a heating rate of 5 °C/min, using a 1/99 vol.%/vol.% $O_2/N_2$ mixture at a flow rate of 25 mL/min.

X-ray diffraction (XRD) measurements were carried out on a D8 Advance Bruker diffractometer in a θ/θ mode and using the $K\alpha_1$ radiation of Cu at 1.5406 Å. The mean $TiO_2$ crystallite size, *i.e.* the average size of the coherent diffracting domains, was determined from the Scherrer equation with the usual assumption of spherical crystallites. The anatase phase in the crystallized samples was identified from the most intense diffraction peaks, *i.e.* the (101) peak at 25.7°, respectively, according to the Nos. 21-1275 JCPDS files. The diffractograms were fitted with the Fullprof software using the "profile matching" method from Le Bail that determined the lattice parameters of the crystal phases.

Transmission Electron Microscopy (TEM) was performed on a CM200 Philips microscope working with a voltage of 200 kV. The sample was sonically dispersed in a chloroform solution before a drop of the solution was deposited onto a copper grid covered by a holey carbon membrane for observation.

Inductively coupled plasma optical emission spectrometry (ICP-OES) was performed on a Varian 720-ES spectrometer at the 'Plateforme d'Analyse' of the Institute Pluridisciplinaire Huber Curien, Strasbourg (France). The samples were previously dissolved in an aqueous solution with $H_2SO_4$ and a $(NH_4)_2SO_4$.

X-Ray Photoelectron Spectroscopy (XPS) characterization was performed on a Multilab 2000 (Thermo) spectrometer equipped with Al Kα anode ($h\nu$ = 1486.6 eV). The energy shift due to electrostatic charging was subtracted using the contamination carbon C1s band at 284.6 eV. The spectra were decomposed assuming contributions with a Doniach–Sunjic shape and a Shirley background subtraction. Sulfur-to-titanium (S/Ti) atomic ratios have been calculated using the sensitivity factors, as determined by Scofield.

UV-Vis absorption spectra of the materials were recorded on a Varian Cary 100 Scan spectrophotometer equipped with a DRA-CA-301 Labsphere diffuse reflectance cell.

IsoElectrical Point (IEP) measurements were performed on a Malvern© ZetaSizer with automatic titration.

Infrared Fourier Transform Spectroscopy (IRTF) was carried out with a Nicolet 205X apparatus working in transmittance mode using a sample/KBr (10/90 wt.%) pellet.

The charge-carrier lifetimes in $TiO_2$ after laser light pulses were determined by microwave absorption experiments using the Time Resolved Microwave Conductivity method (TRMC). The TRMC technique is based on the measurement of the change of the microwave power reflected by a sample, $\Delta P(t)$, induced by its laser pulsed illumination. The relative difference $\Delta P(t)/P$ can be correlated, for small perturbations of conductivity, to the difference of the conductivity $\Delta\sigma(t)$ considering the following equation:

$$\frac{\Delta P(t)}{P} = A\Delta\sigma(t) = Ae\sum_i \Delta n_i(t)\mu_i$$

where $\Delta n_i(t)$ is the number of excess charge-carriers $i$ at time $t$ and $\mu_i$ their mobility. The sensitivity factor $A$ is independent of time, but depends on different factors such as the microwave frequency or the

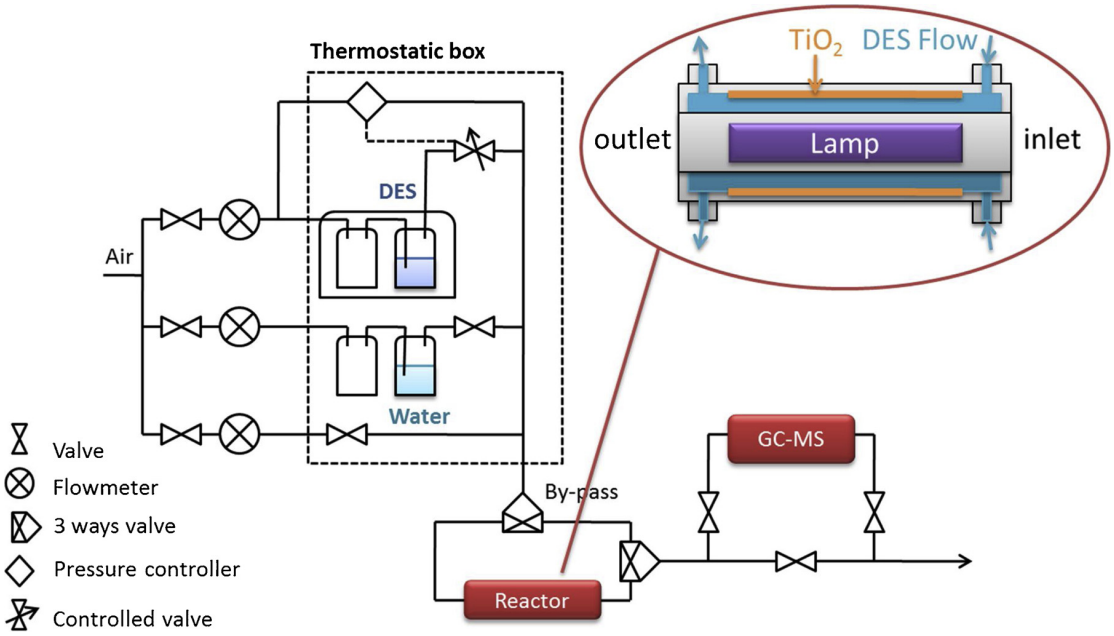


**Scheme 1.** photocatalytic reactor for the elimination of DES.

dielectric constant. Considering that the trapped species have a small mobility, which can be neglected, $\Delta n_i$ is reduced to mobile electrons in the conduction band and holes in the valence band. And in the specific case of $TiO_2$, the TRMC signal can be attributed to electrons because their mobility is much larger than that of the holes.

The incident microwaves were generated by a Gunn diode of the $K_\alpha$ band at 30 GHz. Pulsed light source was an OPO laser (EKSPLA, NT342B) tunable from 225 to 2000 nm. It delivers 8 ns fwmh pulses with a frequency of 10 Hz. The light energy densities received by the sample were respectively 1.2 and 7.0 $mJ{\cdot}cm^{-2}$ at 355 and 450 nm.

The main data provided by TRMC are the maximum value of the signal ($I_{max}$), which indicates the number of the excess charge carriers created by the pulse, including decay processes during the excitation by the laser (10 ns), and the decay (I(t)) due to the decrease of the excess electrons, either by recombination or trapping processes.

## 3. Experimental device and procedure

Gas phase photocatalysis was carried out in a 260 mm length single pass annular Pyrex reactor made of two coaxial tubes 3 mm appart, between which the reactant mixture was passing through (Scheme 1). Extensive details concerning both photocatalytic reactor and device can be found elsewhere. 200 mg of photocatalytic powdered material, corresponding to a reactor surface coverage of 0.48 $mg/cm^2$, was evenly coated on the internal side of the 26 mm diameter internal tube by evaporating a catalyst-containing ethanolic slurry to dryness. The catalyst coated reactor was finally dried at 110 °C for 1 h in air. DES (Aldrich, 98%) and water were fed at ambient temperature and atmospheric pressure by bubbling air through two saturators respectively, and mixed with additional air to obtain the required DES-water-air ratio with a constant total air flow. Standard test conditions under UV activation were chosen for *ca.* 1200 ppmv (*i.e.* 5 g of DES per $m^3$ of flowing air) of DES, 20% relative humidity (RH) and 100 $cm^3$/min under UV-A irradiation. Under solar light irradiation, a concentration of *ca.* 600 ppmv (*i.e.* 2 g of DES per $m^3$ of flowing air) of DES was used, the other experimental parameters being kept constant. 100% of relative humidity was defined as the saturated vapor pressure of water at 25 °C, which corresponds to about 24 Torr, *i.e.* about 3% relatively to the total atmospheric pressure. Before the reaction, the catalyst was first exposed to the reactant-containing air stream with no illumination until dark-adsorption equilibrium was reached. Afterwards the illumination was switched on. Illumination was provided by a commercially available 8-W UV-A black light tube (Philips) with a spectral peak centered around 365 nm (Scheme 2). The total irradiance reaching the $TiO_2$ coating was 8.75 $W/m^2$. In the case of test performed under solar irradiation, a commercially available 24-W lamp (Philips) reproducing the solar spectrum has been used and the total irradiance was 32.7 $W/m^2$ (containing 0.13 $W/m^2$ of UV photons) (Scheme 2). Reactants and reaction products were analyzed *on-line* by an Agilent GC-6890 N Gas Chromatography equipped with HP Plot Q and HP-5MS columns, coupled to a Thermal Conductivity Detector and a MS-5973 N Mass Spectrometer, respectively.

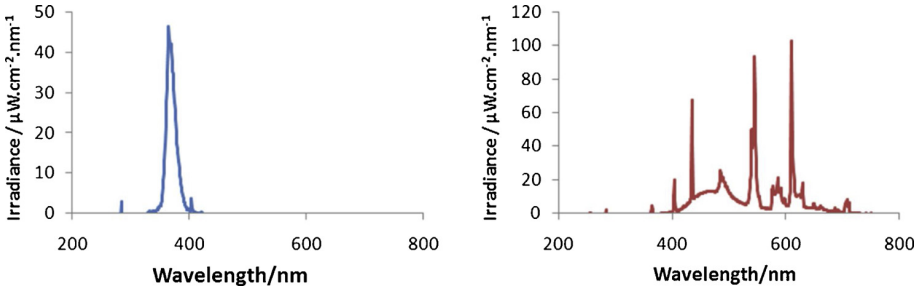


**Scheme 2.** Spectra of UV-A (left) and solar (right) lamps.

**Table 1**
Physico-chemical features of $TiO_2$ and Sn-$TiO_2$ samples.

| Samples | Sn/Ti experimental (wt.%) | $S_{BET}$ ($m^2$/g) | Pore volume ($cm^3$/g) | Particle size from TEM (nm) | Particle size from XRD (nm) |
|---|---|---|---|---|---|
| $TiO_2$(380) | – | 48 | 0.16 | 16 ± 3 | 19 ± 2 |
| 0.5%Sn-$TiO_2$(380) | – | 59 | 0.24 | – | 21 ± 2 |
| 1%Sn-$TiO_2$(380) | – | 64 | 0.18 | 13 ± 4 | 17 ± 1 |
| 4%Sn-$TiO_2$(380) | – | 82 | 0.19 | 10 ± 2 | 13 ± 1 |
| 8%Sn-$TiO_2$(380) | – | 82 | 0.19 | 12 ± 3 | 15 ± 1 |
| $TiO_2$(500) | – | 31 | 0.12 | 30 ± 9 | 29 ± 3 |
| 0.5%Sn-$TiO_2$(500) | – | 34 | 0.14 | – | 23 ± 3 |
| 1%Sn-$TiO_2$(500) | 0.61 ± 0.03 | 38 | 0.21 | 22 ± 7 | 25 ± 1 |
| 4%Sn-$TiO_2$(500) | 2.47 ± 0.09 | 55 | 0.18 | 14 ± 3 | 19 ± 1 |
| 8%Sn-$TiO_2$(500) | 5.80 ± 0.20 | 70 | 0.21 | 12 ± 3 | 15 ± 1 |
| $TiO_2$:PEG(1:1) | – | 31 | 0.12 | – | 20 ± 1 |
| $TiO_2$:PEG(1:2) | – | 22 | 0.06 | – | 14 ± 1 |
| $TiO_2$:PEG(1:7) | – | 55 | 0.23 | – | 13 ± 1 |
| 8%Sn-$TiO_2$:PEG(1:1) | – | 100 | 0.28 | – | 8.9 ± 0.4 |
| 8%Sn-$TiO_2$:PEG(1:2) | – | 75 | 0.53 | – | 10 ± 1 |
| 8%Sn-$TiO_2$:PEG(1:5) | – | 88 | 0.52 | – | 11 ± 1 |
| 8%Sn-$TiO_2$:PEG(1:7) | – | 119 | 0.42 | – | 7.9 ± 0.5 |

## 4. Results and discussions

### 4.1. Photocatalysts characterizations

#### 4.1.1. Elementary analysis

The Sn content of Sn-doped $TiO_2$ samples was measured by ICP-OES (Table 1). The experimental mass ratio of Sn:$TiO_2$ is respectively 0.61 wt.%, 2.47 wt.% and 5.80 wt.% for the theoretical ratio of 1 wt.%, 4 wt.% and 8 wt.%. These results show that there is not much difference between the theoretical and the real values and that the main part of the dopant element was kept in the sample.

#### 4.1.2. Thermogravimetric analysis

The TGA curves of uncalcined samples present three tendencies depending of the presence of Sn and PEG (Fig. 1). The first weight loss below 200 °C can be attributed to the desorption of water in addition to part of dehydroxylation [20] and to the decomposition of the precursors. This loss is more pronounced in the samples containing Sn due to the chlorides elimination. The second huge weight loss stands between 200 and 300 °C and is only visible for the PEG-containing samples. It can be attributed to the decomposition of PEG. The third weight loss after 300 °C can be assigned to the remained products from PEG thermal decomposition and disappears after 480 °C. This behavior was the reason to realize calcination of the PEG-containing materials at 500 °C to avoid the presence of carbon residues.

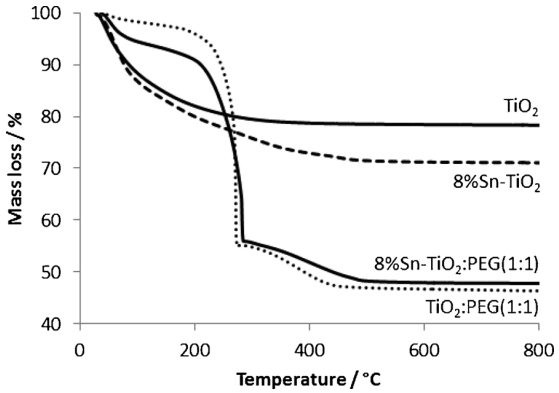


**Fig. 1.** Comparison of TGA weight losses of undoped $TiO_2$ (with and without PEG-$TiO_2$:PEG ratio 1:1) and of 8 wt.% Sn-doped $TiO_2$ (without and with PEG-$TiO_2$:PEG ratio 1:1).

After calcination, the remaining carbon was quantified by measuring the $CO_2$ obtained during a TPO-MS experiment. Residual carbon represents about 0.2 wt.% of the catalyst that can be considered as negligible for our application.

#### 4.1.3. Surface area and porosimetry analyses

The specific surface area and the pore volume of each sample were measured by $N_2$ isotherms at 77 K and the corresponding value are given in Table 1. The isotherms are typical to mainly mesoporous materials and exhibit a type-IV behavior according to the well-admitted classification. For the samples without PEG, the surface area increases from 48 to 82 $m^2$/g with the Sn content and from 31 to 70 $m^2$/g when raising the calcination temperature from 380 °C and 500 °C respectively. The pore volume increases slightly in the same way from 0.16 to 0.19 $cm^3$/g with the Sn concentration and from 0.12 to 0.21 $cm^3$/g with the calcination temperature, respectively. When PEG is added during the sol gel synthesis, the enhancement of the specific surface area and of the pore volume is more pronounced to reach 55 $m^2$/g and 0.23 $cm^3$/g for the undoped-$TiO_2$ sample and 119 $m^2$/g and 0.42 $cm^3$/g for the 8 wt.% Sn-doped $TiO_2$ calcined at 500 °C.

#### 4.1.4. Structural and morphological characterizations

The XRD pattern of Sn-doped nanoparticles without PEG present only the anatase phase (Fig. 2). According to the measurement detection limit, no $SnO_2$ phase was evidenced. The cell parameters and volume of the anatase phase increase proportionally with the Sn amount, as shown in Fig. 3 and Table 2. It must be mentioned that the addition of PEG during the synthesis lead to the appearance of rutile phase (Fig. 4). Furthermore, the rutile contribution is higher in presence of Sn and PEG to reach 47% for a $TiO_2$:PEG ratio of 1:5 (Table 2).

The mean particle size of the materials was determined TEM analysis, respectively and are shown in Table 1. Figs. 5 and 6 present the TEM images of the undoped and Sn-doped materials synthetized without PEG and calcined at 380 °C and 500 °C respectively. One can mention that the particle size diminishes from 16 to 10 nm (calcination at 380 °C) and to 30 to 12 nm (calcination at 500 °C) when the Sn amount increases. It must be underlined that for Sn ratio above 4 wt.%, the particle size is almost the same for the two calcination temperatures. One can also underline that the mean crystallite size determined from XRD pattern are very close to the nanoparticle size determined from TEM. We can thus consider that $TiO_2$ nanoparticles are mainly present in a monocristalline form. By considering this assumption, the size of PEG-modified $TiO_2$ nanoparticles was only measured by XRD. For the undoped nanoparticles, their sizes decrease from 20 to 13 nm (for a $TiO_2$:PEG ratio of respectively 1:1 and 1:7) when PEG ratio increases. One can also observe that Sn-doped samples synthesized with PEG exhibit smaller size than without PEG. The corresponding sizes decreases until 8 nm for a $TiO_2$:PEG ratio of 1:7.

#### 4.1.5. Surface properties

**XPS analysis.** $Ti_{2p}$ XPS spectra [21] displayed the two contributions of $Ti_{2p}^{3/2}$ and $Ti_{2p}^{1/2}$ spin-orbital coupling at 458 and 464 eV for all samples, assigned to $Ti^{4+}$ species in $TiO_2$ structure. No contribution of $Ti^{3+}$ was detected. The $O_{1s}$ signal showed a broad convoluted contribution with a first contribution at 529 eV attributed to Ti-O-Ti surface species [22], a second contribution at 530 eV assigned to surface hydroxyl groups on $TiO_2$ [23] and a third broader contribution at around 531 eV corresponding to adsorbed water. The $Sn_{3d}$ XPS spectra of the undoped-$TiO_2$ samples without PEG modification are given in Fig. 7 and compared with that of pure $SnO_2$. The binding energies of $Sn_{3d}^{5/2}$ and $Sn_{3d}^{7/2}$ orbitals are reported in Table 3. They are measured at 486.4 eV and 494.9 eV for the reference $SnO_2$, thus attributed to $Sn^{4+}$ species in $SnO_2$ environment [24]. For the Sn-doped samples, for better clarity and better determination of the binding energy shifts, we focused only on $Sn_{3d}^{7/2}$ contribution (Fig. 7). One can observe that Sn-

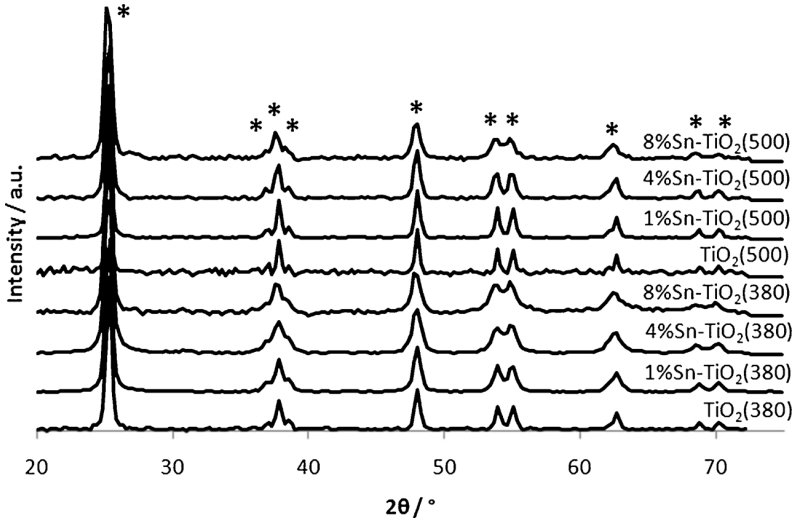


**Fig. 2.** XRD pattern of undoped and Sn-doped nanoparticles calcined at 380 °C and 500 °C, *: anatase.

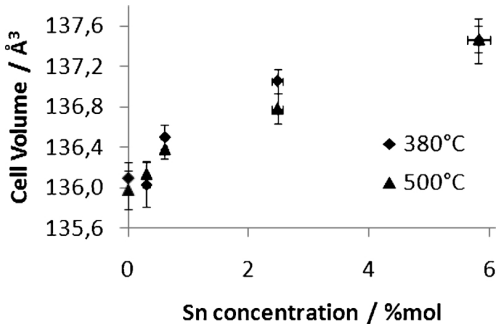


**Fig. 3.** Cell volume of $TiO_2$ anatase calculated with the cell parameters obtained from profile matching of undoped and Sn-doped nanoparticles calcined at 380 °C and 500 °C.

doping results in binding energy shifts of at least 0.4 eV towards lower energies, compared to the reference $SnO_2$. It can thus be argued than Sn atoms the doped samples are not present in the same chemical environment than in $SnO_2$ structure, evidencing the doping. No significant changes were noticed with the PEG-modified samples, certainly due to the removal of PEG during calcination at 500 °C that did not affect the chemical environment of Ti and Sn atoms.

**Zetametry measurements**. The isoelectic point (IEP) was determined at the pH of 4.6 ± 0.1 for the undoped $TiO_2$ sample calcined at 500 °C and at the pH of 3.5 ± 0.1 for the 8 wt.% Sn-doped $TiO_2$ sample calcined at 500 °C, showing that Sn doping leads to increase the surface acidity of the material.

#### *4.1.6. Optical properties*

The bangap values resulting from the analysis of the adsorption spectra of the catalysts are represented in Figs. 8 and 9 for non-modified and PEG-modified materials, and are calculated from the Tauc curve (not represented here). The values lie between 3.2 and 3.0 eV decreasing with Sn concentration, and proving the doping effect. Consequently Sn doping decreases the bandgap by 0.25 eV to reach 2.95 eV (corresponding to an absorption edge of *ca.* 420 nm) which would allow a visible-light use for photocatalytic applications. No supplementary effect was evidenced for PEG-containing samples, meaning that the additional presence of a large contribution of rutile phase due to PEG modification did not lead to additional visible light absorption properties compared to Sn doping. It can thus be concluded that whatever the quantity of PEG the decrease in the bandgap induced by Sn doping does not allow discrimination with the contribution issued from the rutile phase.

**Table 2**
Crystallographic parameters of undoped and Sn-doped $TiO_2$ nanoparticles.

| Samples | Anatase mass ratio (wt.%) | Rutile mass ratio (wt.%) | $a_{anatase}$ (Å) | $c_{anatase}$ (Å) | $V_{anatase}$ (Å$^3$) |
|---|---|---|---|---|---|
| $TiO_2$(380) | 100.0 | – | 3.784 ± 0.002 | 9.503 ± 0.003 | 136.1 ± 0.2 |
| 0.5%Sn-$TiO_2$(380) | 100.0 | – | 3.784 ± 0.002 | 9.502 ± 0.005 | 136.0 ± 0.2 |
| 1%Sn-$TiO_2$(380) | 100.0 | – | 3.788 ± 0.001 | 9.511 ± 0.002 | 136.5 ± 0.1 |
| 4%Sn-$TiO_2$(380) | 100.0 | – | 3.793 ± 0.001 | 9.526 ± 0.002 | 137.1 ± 0.1 |
| 8%Sn-$TiO_2$(380) | 100.0 | – | 3.795 ± 0.002 | 9.543 ± 0.005 | 137.5 ± 0.2 |
| $TiO_2$(500) | 100.0 | – | 3.782 ± 0.002 | 9.505 ± 0.004 | 136.0 ± 0.2 |
| 0.5%Sn-$TiO_2$(500) | 100.0 | – | 3.784 ± 0.001 | 9.508 ± 0.003 | 136.1 ± 0.1 |
| 1%Sn-$TiO_2$(500) | 100.0 | – | 3.786 ± 0.001 | 9.515 ± 0.002 | 136.4 ± 0.1 |
| 4%Sn-$TiO_2$(500) | 100.0 | – | 3.789 ± 0.001 | 9.530 ± 0.003 | 136.8 ± 0.2 |
| 8%Sn-$TiO_2$(500) | 100.0 | – | 3.795 ± 0.001 | 9.545 ± 0.003 | 137.5 ± 0.1 |
| $TiO_2$:PEG(1:1) | 92.9 ± 0.8 | 7.1 ± 0.6 | 3.784 ± 0.001 | 9.509 ± 0.002 | 136.2 ± 0.1 |
| $TiO_2$:PEG(1:2) | ≈ 100.0 | ≈ 0 | 3.788 ± 0.002 | 9.500 ± 0.006 | 136.3 ± 0.2 |
| $TiO_2$:PEG(1:7) | 98.9 ± 0.4 | 1.2 ± 0.2 | 3.786 ± 0.001 | 9.507 ± 0.001 | 136.3 ± 0.1 |
| 8%Sn-$TiO_2$:PEG(1:1) | 81.6 ± 0.3 | 18.4 ± 0.2 | 3.791 ± 0.002 | 9.497 ± 0.005 | 136.5 ± 0.2 |
| 8%Sn-$TiO_2$:PEG(1:2) | 64.3 ± 0.7 | 35.7 ± 0.6 | 3.789 ± 0.002 | 9.482 ± 0.005 | 136.2 ± 0.2 |
| 8%Sn-$TiO_2$:PEG(1:5) | 53.1 ± 0.5 | 46.9 ± 0.5 | 3.784 ± 0.002 | 9.485 ± 0.004 | 135.8 ± 0.2 |
| 8%Sn-$TiO_2$:PEG(1:7) | 68.3 ± 0.4 | 30.7 ± 0.3 | 3.787 ± 0.001 | 9.463 ± 0.002 | 135.8 ± 0.1 |

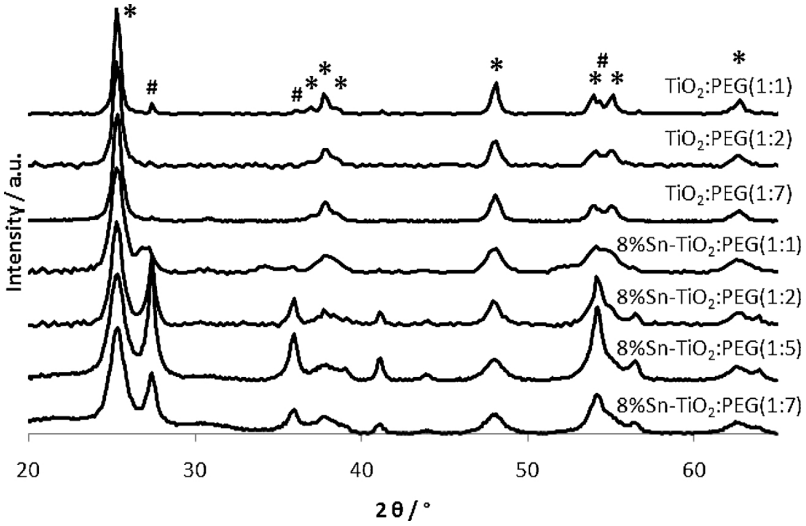


**Fig. 4.** XRD pattern of undoped and Sn-doped nanoparticles synthesized with PEG calcined at 500 °C, *: anatase, #: rutile.

*4.1.7. Electronic properties*

TRMC measurements have been performed under both UV-A (355 nm) and visible light (450 nm) irradiations (Fig. 10) to make also correlation with UV–Vis absorbance measurements and with photocatalytic tests carried out under UV-A and solar irradiation. Electronic properties (charge-carrier dynamics) of Sn-doped $TiO_2$ compounds are given by TRMC measurements gathered in Fig. 10a and b (355 nm) and Fig. 10c and d (450 nm), and Table 3.

At **355 nm irradiation** (Fig. 10 a and b), analyzing the intensity of the signal, one can mention that whatever the calcination temperature, the Sn-doped catalysts present larger intensity than the undoped one, clearly meaning that Sn-doping has a beneficial impact by increasing the number of generated charges. Furthermore, the signal intensity is also dependent on the Sn doping content. The optimal doping concentration is obtained for the lowest doping concentration, *i.e.* 0.5 wt.% and 1 wt.% for calcination temperature of 380 and 500 °C, respectively. Increasing further the Sn content results in a decrease in the generation of charges. The explanation of this phenomenon is not obvious. We can suppose that introduction of intermediate states into the band gap due to different Sn content may modify the bandgap of $TiO_2$ in different manner so that the creation of pair $e^-/h^+$ is more favorable at lower doping ratio. Probably, in this case the doping favors the creation of oxygen deficiency, leading to defects in the crystalline structure of $TiO_2$. Another important parameter to be considered is the decay slope of the signal. The higher the decay, the more important the loss of mobility of the generated electrons, meaning that they are either traps or recombined. One can thus noticed that for the samples calcined at 380 °C, the electron mobility decreases with the increase of the dopant content. This may be correlated with higher charges recombination with the enhancement of the dopant ratio. Indeed, doping may induce defects in $TiO_2$ structure that can also act as recombination centers. Thus, we can argue that if the number of defects raised with the dopant content, it will result in more probable charges recombination. When calcination is performed at 500 °C, one can observe that doping with

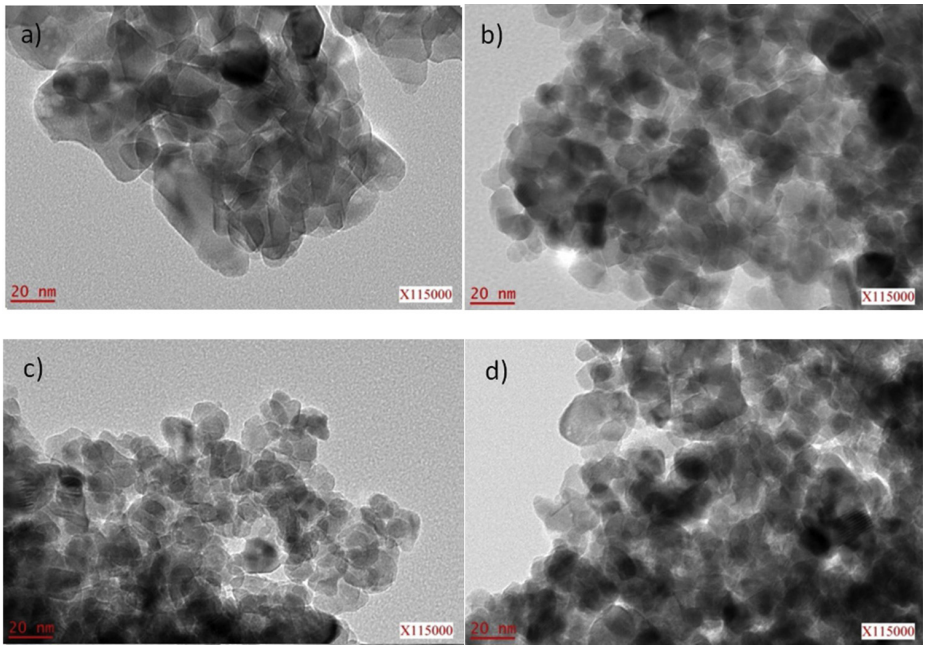


**Fig. 5.** TEM images of undoped and Sn-doped nanoparticles calcined at 380 °C: a) $TiO_2$, b) 1%Sn-$TiO_2$, c) 4%Sn-$TiO_2$, d) 8%Sn-$TiO_2$.

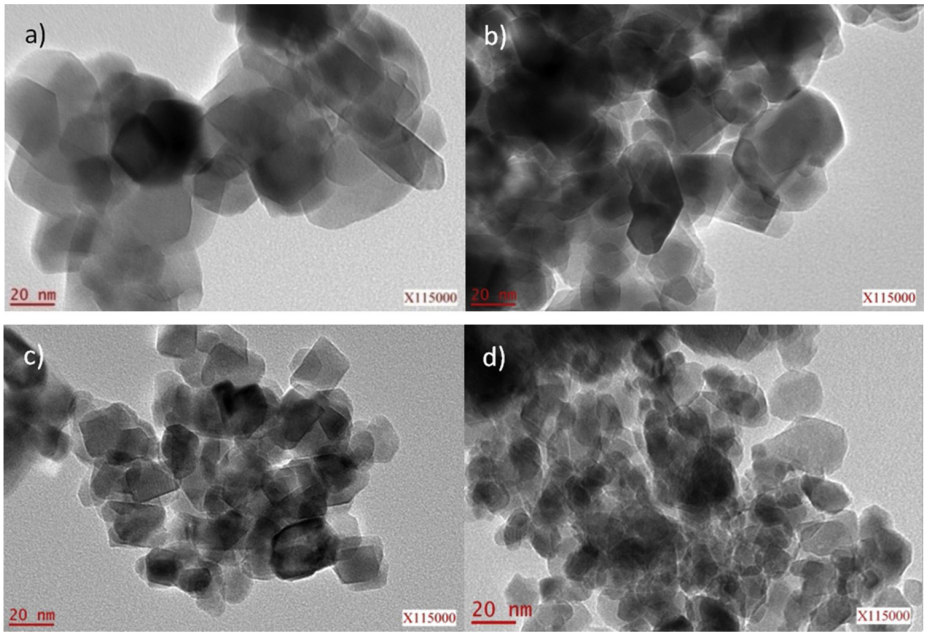


**Fig. 6.** TEM images of undoped and Sn-doped nanoparticles calcined at 500 °C: a) $TiO_2$, b) 1%Sn-$TiO_2$, c) 4%Sn-$TiO_2$, d) 8%Sn-$TiO_2$.

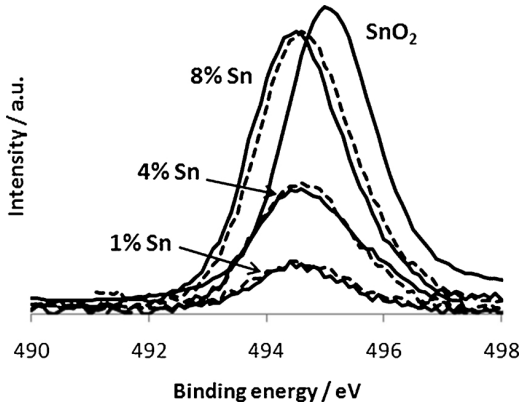


**Fig. 7.** XPS spectra of $Sn_{3d}{}^{7/2}$ region of Sn-doped $TiO_2$ samples calcined at 380 °C (dashed line) and 500 °C (straight line) compared to commercial $SnO_2$.

**Table 3**
binding energy of $Sn_{3d}{}^{5/2}$ and $Sn_{3d}{}^{7/2}$ orbitals.

| Samples | E Sn $3d_{5/2}$ (eV) | E Sn $3d_{7/2}$ (eV) | Sn/Ti on surface from XPS (%mol) | Sn/Ti in volume (%mol) |
|---|---|---|---|---|
| $SnO_2$(500) | 486.4 | 494.9 | – | – |
| 0,5%Sn-TiO2(380) | 485.7 | 494.2 | 0.5 ± 0.2 | 0.34 |
| 0,5%Sn-TiO2(500) | 485.6 | 494.1 | 0.6 ± 0.2 | 0.34 |
| 1%Sn-TiO2(380) | 486.0 | 494.5 | 0.7 ± 0.3 | 0.61 ± 0.03 |
| 1%Sn-TiO2(500) | 485.8 | 494.3 | 1.3 ± 0.5 | 0.61 ± 0.03 |
| 4%Sn-TiO2(380) | 486.0 | 494.5 | 5.3 ± 1.1 | 2.47 ± 0.09 |
| 4%Sn-TiO2(500) | 486.0 | 494.5 | 4.9 ± 1.0 | 2.47 ± 0.09 |
| 8%Sn-TiO2(380) | 486.0 | 494.5 | 9.1 ± 1.0 | 5.8 ± 0.2 |
| 8%Sn-TiO2(500) | 485.8 | 494.3 | 9 ± 1.0 | 5.8 ± 0.2 |

1 wt.% of Sn results in the highest signal but also to the faster decay. We can thus argue that more charges may be generated but they recombine faster. One can also underline that electron recombination or trapping is less marked for the samples calcined at 500 °C. That observation might be correlated with the largest particle size with less defective $TiO_2$ structure when the calcination temperature is increased.

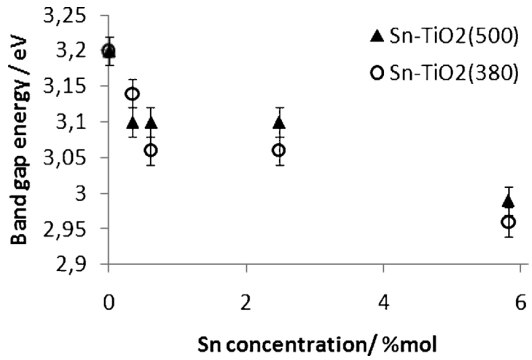


**Fig. 8.** Band gap energy calculated from UV–vis absorbance spectra of Sn-doped $TiO_2$ samples as a function of Sn concentration.

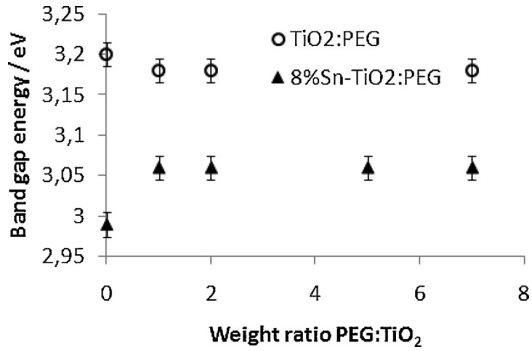


**Fig. 9.** Band gap energy calculated form UV–vis absorbance spectra of undoped and 8 wt.%Sn-doped $TiO_2$ samples according to the PEG ratio.

**At 450 nm** irradiation (Fig. 10c and d), non negligible signal intensities are detected, confirming the positive effect of visible light absorption (in the blue region) resulting from Sn doping. As for UV-A activation, the lowest Sn concentration is correlated with the highest signal. Nevertheless, the lowest Sn content leads to the largest number of photogenerated electrons, whether for calcination at 380 °C or at

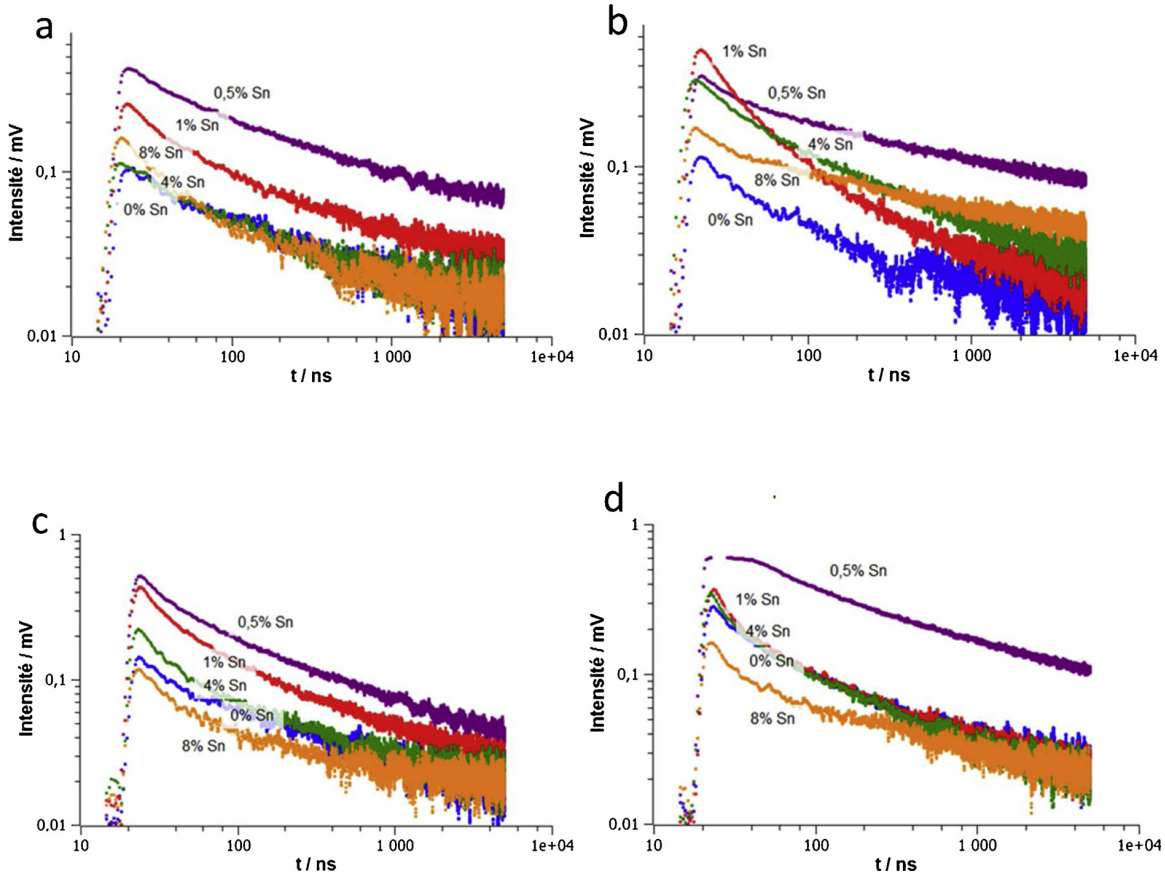


**Fig. 10.** TRMC signal obtained by irradiation of Sn-doped $TiO_2$ a) calcined at 380 °C and excited at 355 nm, b) calcined at 500 °C and excited at 355 nm, c) calcined at 380 °C and excited at 450 nm, d) calcined at 500 °C and excited at 450 nm.

500 °C. As for UV-A activation it also seems that the decay of signal is less important when the samples are calcined at 500 °C compared to 380 °C.

### 4.2. Photocatalytic activity of Sn-$TiO_2$ catalysts

#### 4.2.1. Photocatalytic activity under UV-A illumination

The conversion rates of DES by the Sn-doped catalysts under UV-A illumination are shown in Fig. 11 (calcination at 380 °C) and Fig. 12 (calcination at 500 °C). Each point in Figs. 11–14 corresponds to a value of the DES conversion at a time "t" calculated with the following equation : DES conversion = $C_{DES}$ inlet-$C_{DES}$ outlet/$C_{DES}$ inlet. The activities of these Sn-modified $TiO_2$ materials were compared to that of the reference $TiO_2$ P25 (Evonik) photocatalyst. As already mentioned in previous works [13], the undoped $TiO_2$ sol–gel calcined at 380 °C and 500 °C yield the same lower level of performances. Sn-$TiO_2$ containing 0.5 and 8 wt. % of dopant and calcined at 380 °C exhibit lower photocatalytic activity than the reference $TiO_2$-P25 whereas 4% Sn-$TiO_2$ sample is comparable to the reference. Amongst all the evaluated photocatalysts, 1% Sn-$TiO_2$ reveals the best performance with total DES

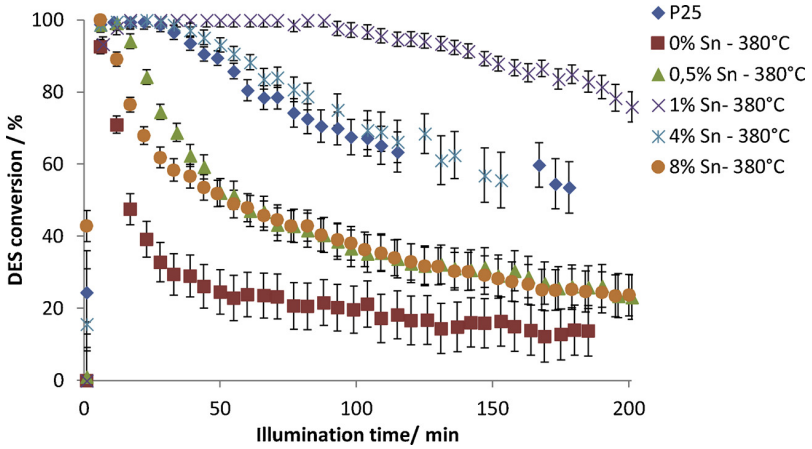


**Fig. 11.** Diethylsulfide conversion under UV-A illumination on Sn-doped $TiO_2$ calcined at 380 °C, influence of Sn content.

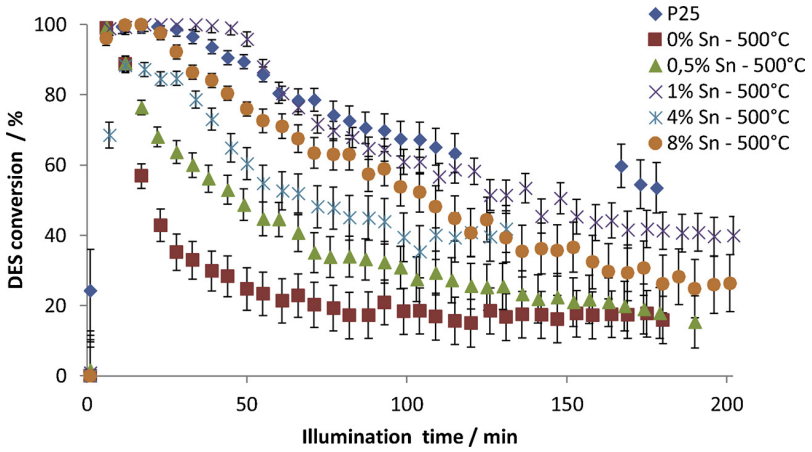


**Fig. 12.** Diethylsulfide conversion under UV-A illumination on Sn-doped $TiO_2$ calcined at 500 °C, influence of Sn content.

elimination over 90 min to reach still 75% after 150 min under flow.

Generally, all the samples calcined at 500 °C reached lower photocatalytic activity compared to $TiO_2$-P25 (Fig. 12), however 1% Sn-$TiO_2$ was slightly better.

As we have previously shown, the BET surface area of the samples calcined at 500 °C are lower than those calcined at 380 °C, which may partly explain the lower activity of this series of photocatalysts. However, the specific area does not explain the results obtained for the different Sn/Ti ratio. Indeed, the most effective sample (1% Sn-$TiO_2$ calcined at 380 °C) has a lower BET value than catalysts doped with 4 and 8 wt. % of Sn (Fig. 11).

In fact, the TRMC measurements have demonstrated high generation of charge carriers for the samples doped with the lowest content of Sn, *i.e* 0.5 wt% when calcined at 380 °C and 1 wt % when calcined at 500 °C, whereas 0.5% Sn-$TiO_2$ material exhibits the poorest photocatalytic properties that may also be associated with lower surface area (47 $m^2/g$ *vs.* 64 $m^2/g$). Consequently it may be argued that the best material associates both higher charges generation and higher surface area. The increase of generated charges and specific area lead to higher performance than non-doped samples synthesized by sol-gel routes. However as the electron/hole pairs recombine rapidly (probably due to the defects in the structures of doped catalysts), all photogenerated charges do not migrate to the surface of $TiO_2$ to oxidize organic pollutants (DES and its by-products), leading to more limited activity. Thus, the only real effective catalyst is the sample containing 1 wt. % of Sn and calcined at 380 °C, knowing that 1 wt. % of Sn catalyst calcined at 500 °C showed a higher charges recombination.

To increase the surface area of the Sn-$TiO_2$ catalysts, we added a porogen template (Polyethylene glycol : PEG) during the synthesis of catalysts. Adding a template during the synthesis enhanced the specific surface areas, confirming that the PEG acted as porogen or porosity promoter. This positive effect is induced by the PEG decomposition during the thermal treatment (see material characterization part). The results of photocatalytic tests with Sn-$TiO_2$ catalysts synthesized with PEG are shown in Fig. 13. The photocatalytic activities of PEG-modified materials are very high and better compared to the $TiO_2$-P25 reference. Doping with Sn together with PEG modification improve significantly the photocatalytic activity. Indeed after 200 min of irradiation under DES continuous flow 60% of DES elimination was obtained against only 25% without PEG addition. Furthermore it can be noticed that the PEG amount has no significant influence on the DES conversion after 200 min. In this case, increasing the specific surface area appears only to delay the beginning of the deactivation (there are more active sites available).

The presence of rutile in contact with anatase (and consequently the formation of heterojunction in the PEG-mofified catalysts may also contribute to improve the photocatalytic performances thanks to better separation of photogenerated charges (limiting the e-/h + recombination).

The following gaseous compounds were quantified to estimate the carbon and sulfur balances at the end of the photocatalytic reaction: $CO_2$, $SO_2$, acetaldehyde (MeCHO) and diethyldisulfide. Because, according to our previous work, these are the only by-products found at the end of reactions (see reference Sn-$TiO_2$). The percentages of carbon

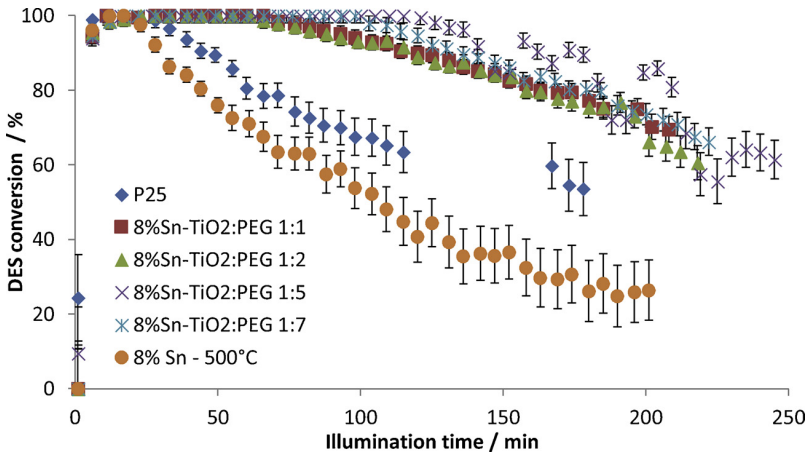


**Fig. 13.** Diethyl sulfide conversion under UV-A illumination on 8%Sn- $TiO_2$ samples calcined at 500 °C : influence of PEG content.

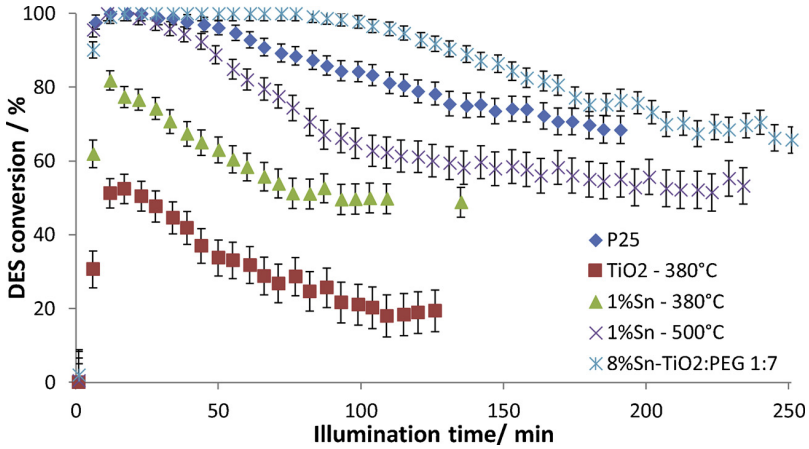


**Fig. 14.** Diethyl sulfide conversion under solar illumination. Influence of Sn content, of calcination temperature and of PEG modification.

**Table 4**
Sulfur and Carbon conversion under irradiation.

| Samples [irradiation] | S conversion in gaseous compounds (%) | C conversion in gaseous compounds (%) |
|---|---|---|
| $TiO_2$-P25 [UV-A] | 23 | 84 |
| $TiO_2$-500 °C [UV-A] | 25 | 99 |
| 1%Sn-500 °C [UV-A] | 36 | 85 |
| 4%Sn-500 °C [UV-A] | 48 | 83 |

and sulfur converted to gaseous compounds for different catalysts for the entire test period (total removal of DES) are shown in Table 4. For all catalysts, less than 50% of the sulfur is converted into gaseous products. Likewise a part of the carbon is not completely converted into gas. This assumes that some of the compounds formed remain adsorbed on the surface of the catalysts.

*4.2.2. Photocatalytic activity under solar irradiation*

The photocatalytic activity of some of the most relevant Sn-$TiO_2$ catalysts was evaluated under solar radiation (Fig. 14). As activity was lower than under UV-A irradiation, testing conditions were less drastic with lower inlet DES concentration (600–700 ppm) at flow rate of 100 $cm^3$/min with a relative humidity of 20%.

From Fig. 14 we observe that the undoped material exhibit the poorest activity that could be strongly enhanced by 1 wt/% Sn doping, those activities remaining however lower than the one obtained on the reference $TiO_2$ P25 sample. It must here be underlined that the additional PEG modification results to a considerable increase in activity to achieve total DES elimination during at least 90 min, followed by deactivation until still 75% conversion after 250 min. It must also be mentioned than the deactivation is less marked than on $TiO_2$ P25. This much better activity under solar irradiation may be explained by the bandgap reduction of Sn-$TiO_2$, due to insertion of intermediate levels in $TiO_2$ anatase (2.95 eV for 8%Sn-$TiO_2$ instead of 3.2 eV for $TiO_2$ anatase) that allows absorption of photons in the beginning of the visible spectrum. Additionally 8%Sn-$TiO_2$:PEG sample presents a high rutile phase contribution (31%) like the $TiO_2$ P25 reference (*ca.* 20%). It must be remind that increasing Sn content led to poorer charges generation, especially under visible light activation at 450 nm (Fig. 10c). However, as the band gap was lowered, the material is able to collect photons from a broader visible light wavelengths window. It may also be argued that the enhancement of surface area due to PEG modification strongly prevents from deactivation phenomena.

## 5. Conclusion

The doping of $TiO_2$ with Sn brings new characteristics to $TiO_2$ that are beneficial for increasing photocatalytic activities under both UV−A and solar irradiation. However, it has been pointed out that an optimal amount of dopant is mandatory. The addition of 1% Sn increases significantly the surface area from 30 to 80 $m^2$/g and decreases the particle size (from 30 nm to 12 nm). In addition, Sn-doping results in a reduction of the anatase band-gap from 3.2 to 2.95 eV, which contributes to generate more charge carriers under UV−A and visible light irradiation. Furthermore, the addition of PEG as a porogen in the synthesis of sol gel $TiO_2$ leads to increase the specific surface, thus limiting. The addition of porogen also promotes the anatase-rutile transition at low calcination temperature, which favors the activity of the catalyst in the visible light range. Those different combined and optimized parameters, allowed us to considerable increase UV−A and solar-light activated DES elimination.

## Acknowledgments

The authors thank the DGA-France (Délégation Générale à l'Armement) for supporting this study. P. Bernhardt (ICPEES-Strasbourg) is acknowledged for performing XPS analyses. L. Vidal (IS2M Strasbourg) is acknowledged for performing TEM analyses

## References

[1] M.A. Fox, Y.-S. Kim, A.A. Abdel-Wahab, Photocatalytic decontamination of sulfur-containing alkyl halides on irradiated semiconductor suspensions, Catal. Lett. 5 (1990) 369–376.
[2] A.V. Vorontsov, A.A. Panchenko, E.V. Savinov, C. Lion, P.G. Smirnotis, Photocatalytic destruction of gaseous diethyl sulfide over TiO2 Appl, Catal. B: Environ. 32 (2001) 11–24.
[3] A.V. Vorontsov, C. Lion, E.N. Savinov, P.G. Smirniotis, Pathways of photocatalytic gas phase destruction of HD simulant 2-chloroethyl ethyl sulfide, J. Catal. 220 (2003) 414–423.
[4] M. Grandcolas, T. Cottineau, A. Louvet, N. Keller, V. Keller, Solar light-activated photocatalytic degradation of gas phase diethylsulfide on WO3-modified TiO2 nanotubes, Appl. Catal. B: Environ. 138 (2013) 138–139.
[5] K.E. O'Shea, S. Beightol, I. Garcia, M. Aguilar, D.V. Kalen, W.J. Cooper, Photocatalytic decomposition of organophosphonates in irradiated TiO2 suspensions, J. Photochem. Photobiol. A: Chem. 107 (1997) 221–226.
[6] A.V. Vorontsov, A.A. Panchenko, E.N. Savinov, C. Lion, P.G. Smirniotis, Photocatalytic degradation of 2-Phenethyl-2-chloroethyl sulfide in liquid and gas phases environ, Sci. Technol. 36 (2002) 5261–5269.
[7] M.A. Fox, Y.-S. Kim, A.A. Abdel-Wahab, M. Dulay, Photocatalytic decontamination of sulfur-containing alkyl halides on irradiated semiconductor suspensions, Catal. Lett. 5 (1990) 369–376.
[8] S. Neatu, V.I. Parvulescu, G. Epure, N. Petrea, V. Somoghi, G. Ricchiardi, S. Bordiga, A. Zecchina, M/TiO2/SiO2 (M = Fe, Mn, and V) catalysts in photo-decomposition of sulfur mustard, Appl. Catal. B: Environ. 91 (2009) 546–553.
[9] C. Cantau, S. Larribau, T. Pigot, M. Simon, M.T. Maurette, S. Lacombe, Oxidation of

nauseous sulfur compounds by photocatalysis or photosensitization, Catal. Today 122 (2007) 27–38.
[10] M. Grandcolas, A. Louvet, N. Keller, V. Keller, Layer-by-Layer Deposited Titanate-Based Nanotubes for Solar Photocatalytic Removal of Chemical Warfare Agents from Textiles, Angew. Chemie Int. Ed. 48 (2009) 161–164.
[11] D. Kozlov, A.V. Vorontsov, P.G. Smirniotis, E.N. Savinov, Gas-phase photocatalytic oxidation of diethyl sulfide over TiO2: kinetic investigations and catalyst deactivation, Appl. Catal. B : Environ. 42 (2003) 77–87.
[12] B. Cojocaru, V.I. Parvulescu, E. Preda, G. Epure, V.E. Somoghi, A.M. Carbonell, M. Alvaro, H. Garcia, Photocatalytic oxidation of gaseous 2-Chloroethyl ethyl sulfide over TiO2, Environ. Sci. Technol. 42 (2008) 4908–4913.
[13] A. Sengele, D. Robert, A. Herissan, C. Colbeau-Justin, N. Keller, V. Keller, Ta-doped TiO2 as photocatalyst for UV-A activated elimination of chemical warfare agent simulant, J. Catal. 334 (2016) 129–147.
[14] M. Xu, P. Da, H. Wu, D. Zhao, G. Zheng, Controlled Sn-Doping in TiO2 nanowire photoanodes with enhanced photoelectrochemical conversion, Nano Lett. 12 (2012) 1503–1508.
[15] F. Sayilkan, M. Asilturk, P. Tatar, N. Kiraz, S. Sener, E. Arpac, H. Sayilkan, Photocatalytic performance of Sn-doped TiO2 nanostructured thin films for photocatalytic degradation of malachite green dye under UV and VIS-lights, Mater. Res. Bull. 43 (2008) 127–134.
[16] I. Bedjat, P.V.J. Kamat, Capped semiconductor colloids. Synthesis and photoelectrochemical behavior of TiO2 capped SnO2 nanocrystallites, Phys. Chem. 99 (1995) 9182–9188.
[17] M. Grandcolas, M. Karkmaz-Le Du, F. Bosc, N. Keller, V. Keller, Porogen template assisted TiO2 rutile coupled nanomaterials for improved visible and solar light photocatalytic applications, Catal. Lett. 23 (2008) 65–71.
[18] B. Banerjee, V. Amoli, A. Maurya, A.K. Sinha, A. Bhaumik, Nanoscale Green synthesis of Pt-doped TiO2 nanocrystals with exposed (001) facets and mesoscopic void space for photo-splitting of water under solar irradiation, Nanoscale 7 (2015) 10504–10512.
[19] B.-L. Su, C. Sanchez, X.-Y. Yang, Hierarchical Structured Porous Materials. From Nanoscience to Catalysis, Separation, Optics, Energy and Life Science, Wiley-CVH verlag, 2012.
[20] M.A. Fox, M.T. Dulay, Heterogeneous photocatalysis, Chem. Rev. 93 (1993) 341.
[21] PhD Dissertation Armelle SENGELE, University of Strasbourg, 2015.
[22] B.F. Dzhurinskii, D. Gati, N.P. Sergushin, V.I. Nefedov, Y.V. Salyn, X-ray electron investigations of some element oxides, Russ. J. Inorg. Chem. 20 (1975) 2307.
[23] D. Costa, P. Marcus, W.P. Yang, Resistance to Pitting and Chemical Composition of Passive Films of a Fe-17%Cr Alloy in Chloride-Containing Acid Solution, Journal Electrochem, Soc. 10 (1994) 2669.
[24] D. Briggs, M.P. Seah, second edition, Practical Surface Analysis vol. 1, John WILLEY and SONS, 1993.